

Improved In Situ Characterization of Electrochemical Interfaces Using Metasurface-Driven Surface-Enhanced IR Absorption Spectroscopy

Luca M. Berger, Malo Duportal, Leonardo de Souza Menezes, Emiliano Cortés, Stefan A. Maier, Andreas Tittl,* and Katharina Krischer*

Electrocatalysis plays a crucial role in realizing the transition toward a zero-carbon future, driving research directions from green hydrogen generation to carbon dioxide reduction. Surface-enhanced infrared absorption spectroscopy (SEIRAS) is a suitable method for investigating electrocatalytic processes because it can monitor with chemical specificity the mechanisms of the reactions. However, it remains difficult to detect many relevant aspects of electrochemical reactions such as short-lived intermediates. Herein, an integrated nanophotonic-electrochemical SEIRAS platform is developed and experimentally realized for the in situ investigation of molecular signal traces emerging during electrochemical experiments. A platinum nano-slot metasurface featuring strongly enhanced electromagnetic near fields is implemented and spectrally targets the weak vibrational mode of the adsorbed carbon monoxide at $\approx 2033\text{ cm}^{-1}$. The metasurface-driven resonances can be tuned over a broad range in the mid-infrared spectrum and provide high molecular sensitivity. Compared to conventional unstructured platinum films, this nanophotonic-electrochemical platform delivers a 27-fold improvement of the experimentally detected characteristic absorption signals, enabling the detection of new species with weak signals, fast conversions, or low surface concentrations. By providing a deeper understanding of catalytic reactions, the nanophotonic-electrochemical platform is anticipated to open exciting perspectives for electrochemical SEIRAS, surface-enhanced Raman spectroscopy, and other fields of chemistry such as photoelectrocatalysis.

1. Introduction

Electrochemical reactions underpin many technologies ubiquitous for a future carbon-zero world such as green-hydrogen generation for long-term sustainable energy storage^[1] and CO₂ degradation to combat the current trends of climate change.^[2] Unfortunately, in general, the monitoring, and therefore understanding, of many electrochemical reactions remains a challenge. In particular, resolving the electrochemical CO₂ reduction reaction (CO₂RR) with high efficiency, selectivity, and sensitivity remains an issue^[3] especially due to the competition with the hydrogen evolution reaction at high current densities.^[4] During the CO₂RR to desired carbon products, a compulsory step to the key intermediate CO is still not fully understood and requires further investigation.^[5]

For the detection and characterization of molecules, optical spectroscopy, mass spectrometry, chromatography, and fluorescence microscopy are often used.^[6] Provided that analyte concentrations are high enough, optical spectroscopy


L. M. Berger, L. d. S. Menezes, E. Cortés, S. A. Maier, A. Tittl
Faculty of Physics
Ludwig-Maximilians-Universität München
80539, München, Germany
E-mail: Andreas.Tittl@physik.uni-muenchen.de

M. Duportal, K. Krischer
Department of Physics
Technical University of Munich
85748, Garching, Germany
E-mail: krischer@tum.de

L. d. S. Menezes
Departamento de Física
Universidade Federal de Pernambuco
Recife-PE 50670-901, Brazil

S. A. Maier
School of Physics and Astronomy
Monash University
Clayton, Victoria 3800, Australia

S. A. Maier
Department of Physics
Imperial College London
London SW7 2AZ, UK

 The ORCID identification number(s) for the author(s) of this article can be found under <https://doi.org/10.1002/adfm.202300411>.

© 2023 The Authors. Advanced Functional Materials published by Wiley-VCH GmbH. This is an open access article under the terms of the Creative Commons Attribution License, which permits use, distribution and reproduction in any medium, provided the original work is properly cited.

DOI: 10.1002/adfm.202300411

methods, such as infrared (IR) or Raman spectroscopy, are highly advantageous because they allow for the retrieval of the spectral fingerprint of molecules via the detection of their rotational or vibrational modes. Unfortunately, during electrochemical reactions, most adsorbed intermediates occur in low concentrations and limit their detection with conventional spectroscopic techniques.^[7,8] Surface-enhanced IR absorption spectroscopy (SEIRAS) is a derivative technique from conventional IR spectroscopy based on the enhancement of the local electromagnetic (EM) near fields. To increase the sensitivity of SEIRAS during electrochemical reactions typically a rough metal surface has been chosen to enhance the local electromagnetic near fields.^[9] Rough and highly disordered metallic nm-sized edges coming from perforations and extrusions in the metallic film locally confine and enhance the EM fields. Unfortunately, this approach is random, does not allow for spectral tailoring of plasmonic hotspots, and consequently generates a relatively weak EM near-field enhancement. Even after improvements in the sensitivity of SEIRAS using an attenuated total internal reflection (ATR) geometry,^[7,8] the characterization of CO adsorption on catalysts is still hampered by weak signal traces.^[10–12]

We overcome the challenge of detecting weak signal traces by taking inspiration from other fields of nanophotonics. In biomolecular sensing, a plethora of alternatives are used to improve molecular detection using controlled and tuneable EM near-field enhancement via the excitation of resonances through tailored system parameters on the nanoscale. Examples are plasmonic nanoparticles, non-plasmonic nanogap dimers,^[13] metasurfaces based on plasmonics^[14] or exotic phenomena like quasi-bound states in the continuum,^[15] waveguides^[16] or 2D-integrated^[17] platforms, among others.^[18] Plasmonic-based sensors have become the method of choice in label-free detection of biomolecules. They can be used either as 1) refractive index sensors or 2) by coupling the resonances to the molecular modes and analysing the perturbation of the intensity either in reflection or transmission,^[19] termed perturbed intensity sensing here.

In fact, some recent progress has been made to integrate plasmonic structures for refractive index sensing with electrochemistry.^[19–21] There are also recent examples of plasmonic structures for perturbed intensity sensing for surface enhanced Raman spectroscopy used to monitor electrochemical reactions^[22] or to study the mechanism of an electrocatalytic reaction.^[23] Literature of plasmonic imaging provides other examples of electrochemical reactions of single nanoparticles,^[24] plasmonics-supported and electrochemical monitoring of molecular interactions focused on fluorescence and confocal microscopy,^[25,26] and plasmon-accelerated electrochemical reactions.^[27,28] However, to the best of our knowledge, the integration of nanostructured metasurfaces for perturbed intensity sensing in SEIRAS has never been shown in combination with electrochemistry.

Here, we detect in situ the CO vibrational mode at 2033 cm⁻¹ emerging during the electrochemical conversion of CO into CO₂ using a platinum nano-slot metasurface on a CaF₂ substrate (Figure 1a) by coupling its resonance to the molecular vibrational mode and analyzing the perturbation of the intensity in reflection. We investigated the vibrational mode of

linearly adsorbed CO on platinum (CO_{linear}) at 2033 cm⁻¹ because it is the most intense vibrational mode of CO on platinum.^[29–33] The material of choice was platinum as it could fulfill all requirements, namely to function as a working electrode, support strong metasurface-driven resonances, and adsorb CO on its surface.^[34] Moreover, Pt is a catalytic material for many reactions, making this platform very useful not only for the CO oxidation reaction but also for other reactions. The decision on the inverse structure (i.e., the slots), was made to preserve a connected metallic film that can carry electrical current. The nano-slots feature nanorod-like resonances as predicted by Babinet's principle. Babinet's principle predicts that if a structure features a resonance in transmission (reflection) under a certain polarization of the incident light its inverse structure will feature a similar resonance in reflection (transmission) under a 90° change in polarization as long as their geometrical parameters are the same.^[35] Nano-slots can be tuned to enhance the electric and magnetic near-fields due to the excitation of a magnetic dipole aligned parallel to the long axis of the slot.^[35] Consequently, a strong extended hot spot of the electric field is compressed inside the slot. Therefore, compared to resonant rod-type antennas, the inverse counterparts have been shown to feature superior detection of molecular signal traces due to linearly instead of exponentially decaying EM near-fields and single hot spot being more extended.^[35] The slots can only be excited with transverse electric (TE) or s-polarized light.^[35] We perform SEIRAS in an ATR geometry to further improve the sensing performance while maintaining free accessibility of the electrode surface for reactants and products, and to minimize the contribution of the electrolyte to the IR spectrum.^[7,8] We confirm the detection of adsorbed CO via the observation of the typical Stark shift and resolve a so far scarcely studied^[36–38] effect due to the decrease of the CO coverage on the surface of platinum during the electrochemical oxidation. Furthermore, the presence of a second peak at 2086 cm⁻¹ on the spectral location of the linear vibrational mode could be attributed to the effect of the crystal orientation. Finally, we establish a methodology for designing similar nanophotonic-electrochemical platforms.

2. Results and Discussion

2.1. Numerical Design of Catalytic Nano-Slot Metasurface

We start the implementation of our electrochemical sensing platform with the numerical design of the chosen nano-slot metasurface geometry. The structure consists of a unit cell composed of a single slot in an otherwise connected platinum film submerged in water on CaF₂ (Figure 1b). Notably, we model adsorbed CO by including an artificially created material covering the inside walls parallel to the long axis of the slot. The choice for the parameters of the unit cell was guided by Huck et al.^[35] and modified in accordance with fabrication constraints. Huck et al.^[35] optimized a gold nano-slot metasurface in the mid-IR for normal incidence illumination in air for high-quality factors (Q-factors) and electric near fields. The Q-factor relates the initial energy stored in a resonator to the energy dissipated in one radian of the cycle of oscillation.^[39]

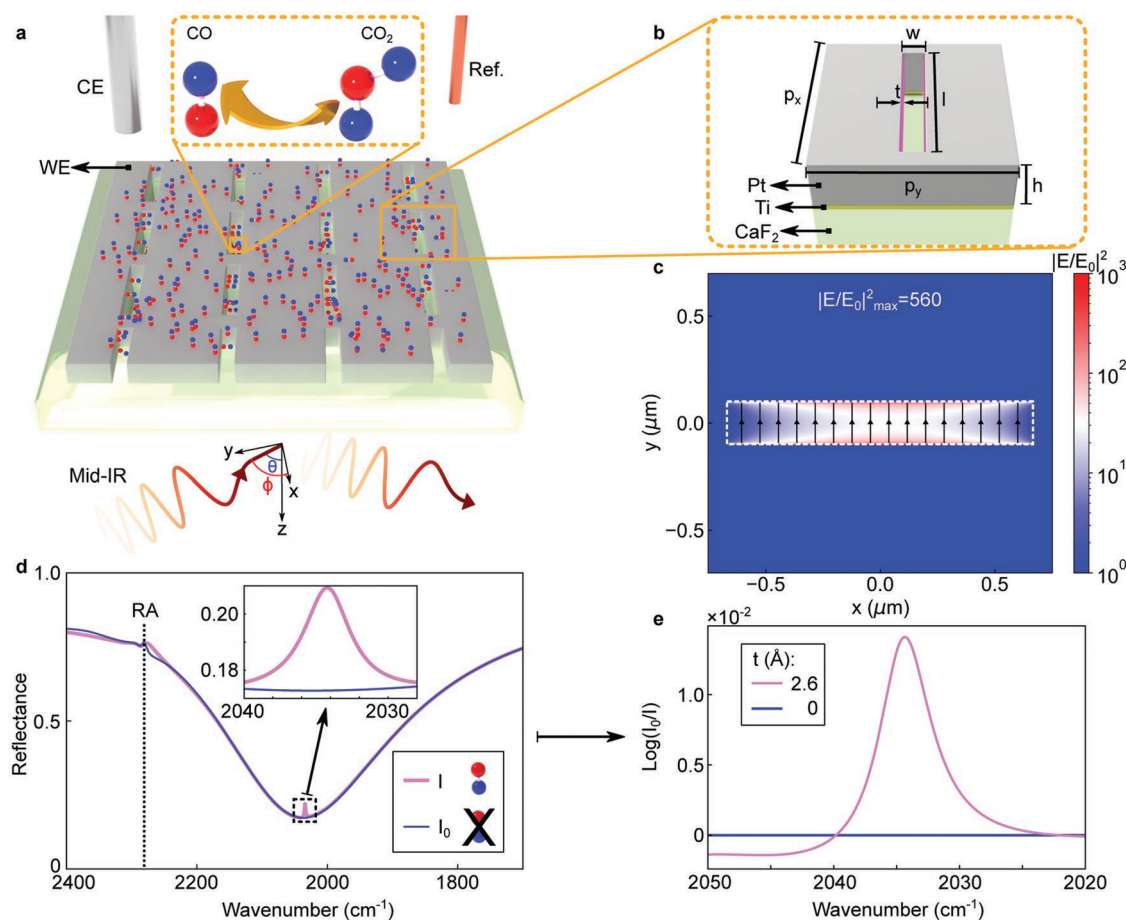


Figure 1. Numerical design of the catalytic metasurface. a) Schematic for the Pt-based nano-slot metasurface for the in situ integrated nanophotonic-electrochemical study of CO oxidation. As the potential between the working electrode (WE) and the reference electrode (ref.) is swept the presence of adsorbed CO is monitored via the detection of the linear vibrational mode of CO at 2033 cm^{-1} with a Fourier transform infrared (FTIR) spectrometer. The nano-slot metasurface enhances the electromagnetic near-fields of TE polarized light in an ATR configuration coming in at an azimuthal angle $\phi = 0^\circ$ and polar angle $\theta = 72^\circ$ w.r.t. the Pt film (xy -plane). b) Sketch of the Pt on CaF_2 nano-slot unit cell. Two CO model layers were included parallel to the long edges of the slot (magenta) with dimensions $l \times h \times t$. A 1 nm thick Ti adhesion layer was used in the fabrication of the structures but is not considered in the numerical simulations due to its negligible effect on the resonance position. The geometrical parameters of the unit cell for (c), (d), (e) are $h = 30\text{ nm}$, $w = 200\text{ nm}$, $l = 1380\text{ nm}$, $p_y = 1400\text{ nm}$, $p_x = 1600\text{ nm}$. In (c) no CO model layer was included. c) Electric near field intensity (taken at $h = 30\text{ nm}$) of the unit cell including arrows (black) showing the direction of the electric field inside the slot. The maximum near field intensity is 560. d) The simulated reflectance spectrum of the metasurface with (pink) and without (blue) the CO model layer ($t = 5\text{ nm}$). The spectrum includes the Rayleigh anomaly (RA). e) The differential absorbance with no CO (blue) compared to a 2.6 Å thick CO layer (pink) showing clearly visible absorption bands.

On the basis of our simulations, the nano-slot metasurface achieves a resonance with a modulation in the absorbance of over 82% and a Q-factor of ca. 6.3 (see Experimental Section for details on the Q-factor calculation). Furthermore, the metasurface numerically exhibits an electric near-field intensity enhancement $|E/E_0|^2$ of 560. This value can be increased in future experiments by decreasing the width of the slots^[35] but was limited here due to fabrication constraints. The maximum electric near-field enhancement occurs inside the slots close to the faces parallel to its long axis (Figure 1c), with its electric field pointing orthogonally to it. The parameters of the unit cell of the nano-slot metasurface are defined in Figure 1b, where p_x and p_y are the unit cell lengths in x and y . l , w , and h are respectively the length, width, and height of the slot, and t is the thickness of the molecular layer used to model adsorbed CO. The gap g between two slots in x is $g = p_x - l$.

Huck et al.^[35] found that the highest Q-factor and electric near field enhancement occurs when w is small, $p_y = \lambda_{\text{res}}/2$, and $g = \lambda_{\text{res}}/2$, where λ_{res} is the central wavelength of the resonance. However, to satisfy the experimental conditions the nano-slot metasurface was simulated in water instead of air, and for an angle of incidence $\theta = 72^\circ$. Under these conditions, tuning the resonance to $2033\text{ cm}^{-1} \approx 4.92\text{ }\mu\text{m}$ leads to the appearance of a Rayleigh anomaly (RA) such that $\lambda_{\text{RA}} > \lambda_{\text{res}}$, where λ_{RA} is the central wavelength of the RA. The RA is a phenomenon associated with light diffracted parallel to the surface of a periodic structure.^[40] When $\lambda_{\text{RA}} > \lambda_{\text{res}}$, the resonance lifetime and electric near-field enhancement is strongly reduced.^[41] Consequently, a metasurface where $\lambda_{\text{RA}} > \lambda_{\text{res}}$ will exhibit poor sensing performance. For this reason, g was reduced to 220 nm to push the resonance on the evanescent side of the RA (Figure 1d).

In coupled-resonator systems, the excitation efficiency of a resonator is significantly dependent on the ratio of its losses to external radiation γ_e , i.e., light scattering, and intrinsic material absorption γ_i which strongly depends on the system design and parameters chosen^[42]. When $\gamma_e \sim \gamma_i$ the system is critically coupled and the second oscillator will lead to a dip in the absorption cross section. SEIRAS performance can be maximized by utilizing a system that is close to the critical coupling condition.^[42,43] Here, the nano-slot metasurface is near the critical-coupling condition with $\gamma_e/\gamma_i = 1.2$. Thus, when the resonance overlaps with the vibrational mode of adsorbed CO at 2033 cm^{-1} the coupling between the two resonators leads to a small peak in the reflectance spectrum (Figure 1d), where t was set to 5 nm as an example to visualize the modulation of the resonance. The differential absorbance is defined as $\log(I_0/I)$, where I and I_0 are the reflectance measured with and without

a CO model molecular layer, respectively (Figure 1c), were used to extract the signal traces of adsorbed CO. To obtain a more realistic expectation for the differential absorbance resulting from adsorbed CO on the nano-slot metasurface, the CO layer was modeled with a thickness of 2.6 \AA (Figure 1e) in agreement with the literature.^[44]

2.2. Metasurface Characterization

First, the effect of the metasurface-driven resonance position on the coupling with the vibrational mode of $\text{CO}_{\text{linear}}$ is studied in ATR mode using a focal plane array detector (Figure 2a). To test our nanophotonic-electrochemical platform, we first tuned the resonance position to match the vibrational mode of $\text{CO}_{\text{linear}}$ in $0.5\text{ M K}_2\text{CO}_3$ saturated with carbon monoxide. Then,

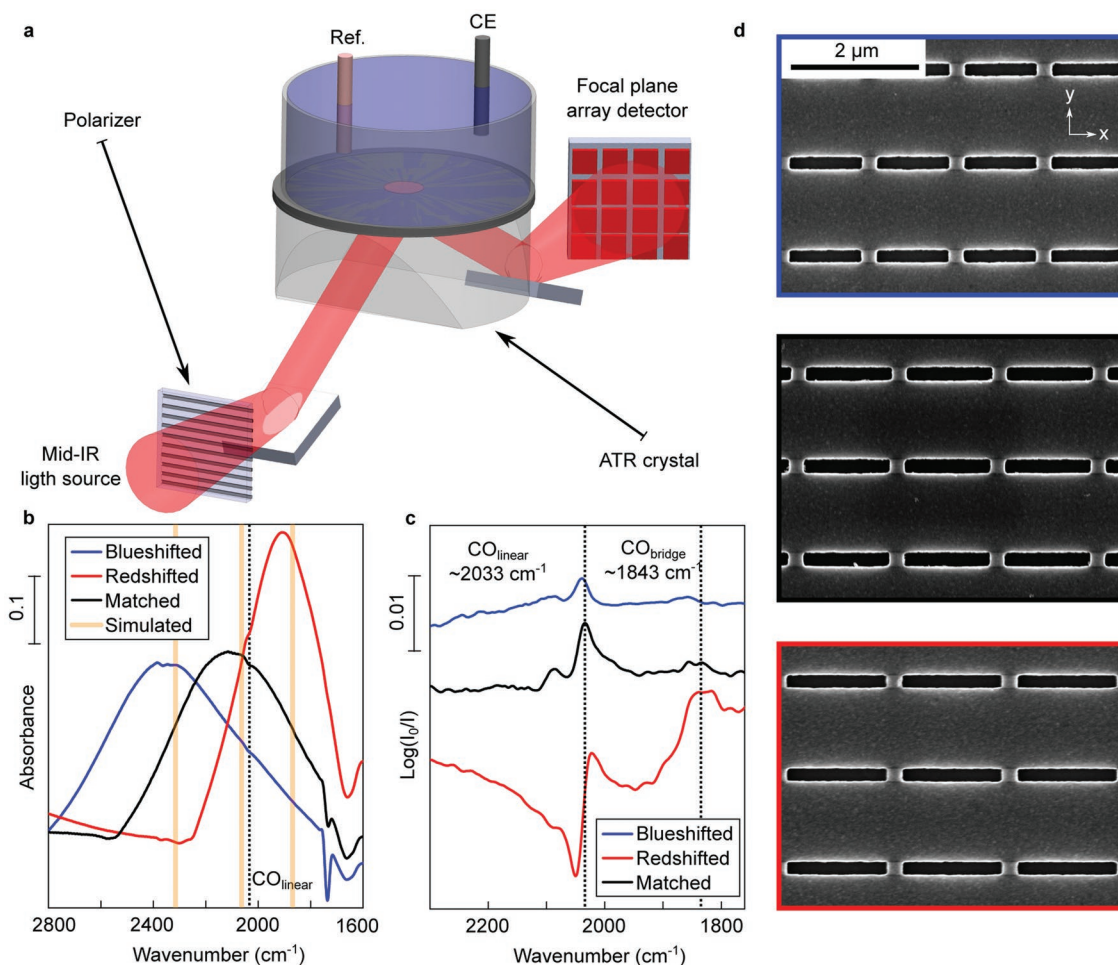


Figure 2. Testing the nanophotonic-electrochemical platform. a) A schematic showing the experimental setup used to perform SEIRAS in an ATR geometry. A continuous mid-IR collimated linearly polarized light source illuminated the nano-slot metasurface from below at an angle of ca. 72° . A focal plane detector array was used to collect the signal. b) Experimental absorbance spectra of three Pt nano-slot metasurface in CO saturated $0.5\text{ M K}_2\text{CO}_3$ aqueous electrolyte interfaces with resonance positions around the ideal position of the vibrational mode of $\text{CO}_{\text{linear}}$ with slot lengths l $1.33\text{ }\mu\text{m}$ (black, ideal) and two detuned resonance positions with slots length of $1.13\text{ }\mu\text{m}$ (blue) and $1.53\text{ }\mu\text{m}$ (red). The other parameters are $h = 30\text{ nm}$, $w = 200\text{ nm}$, $p_y = 1440\text{ nm}$, $\text{gap} = p_x - l = 220\text{ nm}$. The resonance position of $\text{CO}_{\text{linear}}$ is indicated by the black dashed line. The numerically modeled resonance positions at 2312 , 2066 cm^{-1} , and 1876 cm^{-1} (yellow) are shown for comparison. c) The differential absorbance of the CO signal after baseline correction for the blueshifted, matched, and redshifted resonances. d) Scanning electron microscopy images corresponding to the nano-slot metasurfaces used in (b) and (c).

we detuned the resonance to the blue and red spectral regions by decreasing and increasing the slot length l by 200 nm from 1.33 μm , respectively (Figure 2b). There is a good fit between the numerically and experimentally obtained resonance positions, with a discrepancy of less than 40 cm^{-1} . As predicted by the simulations, a dip is observed in the resonance attributed to the vibrational mode of $\text{CO}_{\text{linear}}$. The Q-factor of the experimentally measured metasurface-driven resonance matching this mode (Figure 2b) is 2.9 which is slightly lower than the simulated value. The smaller experimental Q-factor is due to fabrication imperfections compared to the ideal numerical model.^[45] Following these results, slots with a length of ca. 1.33 μm were found to match the vibrational mode of $\text{CO}_{\text{linear}}$. According to the literature^[29–33,46] this mode should be spectrally located between 2020 and 2080 cm^{-1} . On the basis of our experiments, $\text{CO}_{\text{linear}}$ is located at 2033 cm^{-1} .

The differential absorbance highlights a more intense and well-defined $\text{CO}_{\text{linear}}$ signal for the sample which has the best spectral overlap (Figure 2c). Two peaks can be observed at 2033 and 2086 cm^{-1} . The CO signals have a Fano-type line shape due to the narrow discrete nature of the vibrational mode of $\text{CO}_{\text{linear}}$ interfering with the broad spectral line of the metasurface-driven resonance.^[47] The redshifted sample yields a highly asymmetric CO signal due to the strongly off-resonance coupling between

the resonance and the vibrational mode of $\text{CO}_{\text{linear}}$.^[48] In addition, the redshifted sample presents a strong peak $\approx 1843 \text{ cm}^{-1}$, which is attributed to a second configuration of adsorption, the CO bridge ($\text{CO}_{\text{bridge}}$).^[29,30,32,46] The scanning electron microscopy images show good quality of the fabricated nanostructures (Figure 2d). For the next part of this work, the electrochemical behavior of the sample with matching spectral overlap of its resonance with the vibrational mode of $\text{CO}_{\text{linear}}$ is studied.

2.3. CO Adsorption at Open Circuit Potential

Here, we follow in situ the CO adsorption during the saturation of an electrolyte at open circuit potential (OCP) and characterize the CO adsorption by performing SEIRAS concurrently with electrochemical cyclic voltammetry. The transition from the argon-saturated (Ar^{sat}) to the CO-saturated (CO^{sat}) electrolyte is accompanied by a shift of the OCP due to a change of the equilibrium determining redox reaction (Figure 3a). At the equilibrium potential of the Ar saturated electrolyte (ca. 1000 mV_{RHE}) CO is oxidized and the OCP drops towards negative values where CO adsorbs on the Pt surface.

The SEIRAS measurements were taken in 0.5M K_2CO_3 with and without CO using s-polarized light (Figure 3b). Looking

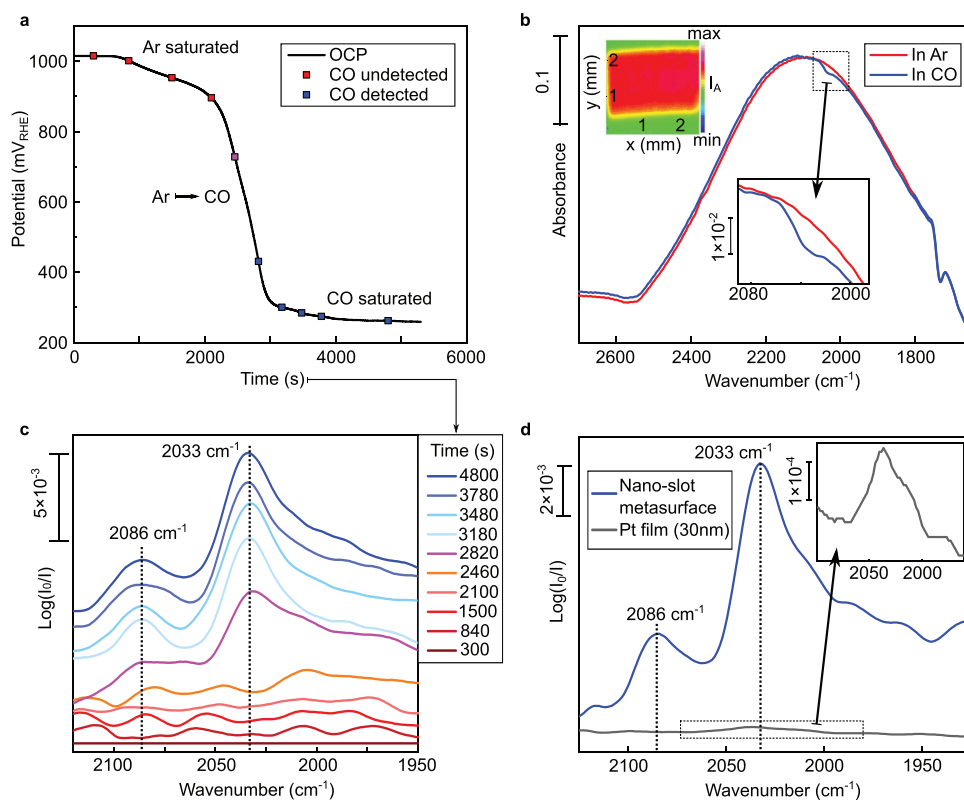


Figure 3. Electrochemical and spectroscopic response of the nanophotonic platform at the OCP during a gas transition from an Ar-saturated electrolyte to a CO-saturated one. a) The evolution of the OCP of the platinum nano-slot metasurface during the transition from an argon-saturated ($\text{Ar}^{\text{sat}} \approx 1000 \text{ mV}_{\text{RHE}}$) to a CO-saturated ($\text{CO}^{\text{sat}} \approx 260 \text{ mV}_{\text{RHE}}$) electrolyte. b) FTIR spectra taken with s-polarized light of the Pt nano-slot metasurface/electrolyte interface in Ar^{sat} and CO^{sat} electrolyte. The heat map represents the integrated area below the resonance between 2600 and 1800 cm^{-1} collected by an array of 64 by 64 detectors. c) The evolution of the differential absorbance $\text{CO}_{\text{linear}}$ peaks during the CO bubbling process. d) Comparison of $\text{CO}_{\text{linear}}$ signals obtained in CO^{sat} electrolyte after 80 min of CO bubbling with a pure Pt layer (p-polarized light) and with the nanophotonic-electrochemical platform (s-polarized light).

at the differential absorbance (Figure 3c), a distortion of the baseline appears at 2460 s (725 mV_{RHE}). Then, after ca. 2800 s (430 mV_{RHE}) two clearly distinguishable CO_{linear} peaks emerge. These peaks become more discernible with time as the coverage of adsorbed CO increases. As the intensity of the peaks stabilizes the maximum coverage of CO is reached.

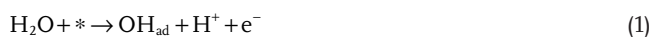
The CO signal obtained with the nano-slot metasurface compared to that obtained with a pure platinum layer (30 nm) at the OCP is increased by an estimated factor of 27 (Figure 3d). Both samples have been evaporated simultaneously. This gives both systems the same material properties such as surface roughness. For this reason, the 27-fold difference between the signals obtained with the two systems can be directly linked to the metasurfaces-driven enhancement provided by nanostructuring the surface of the working electrode.

For adsorbed CO to interact with incident light, the orientation of the transition dipole moment of the CO vibrational mode relative to the electric field component needs to be non-zero.^[49] Consequently, only the (interior) side walls parallel to the long axis of the slots can be considered active representing a ratio of active to total surface of 3.6% compared to a smooth platinum layer. This leads to an experimentally determined local signal enhancement of above 700.

The second peak at 2086 cm⁻¹ was only observed using the nano-slot metasurface. The most likely explanation could be that the higher resolution achieved with the nano-slot metasurface allows for the deconvolution of this peak from the background, which was not possible in previous architectures based on a continuous Pt film. According to the literature, several possibilities exist. The first assumption is that CO could adsorb on different crystal orientations with different binding energies.^[46,50] As reported by A. Cuesta et al.,^[50] adsorption on Pt(111) single crystals were found at ≈2070 cm⁻¹,^[36,50,51] while CO adsorbed on Pt(100) electrodes was detected between 2027 cm⁻¹^[52,53] and 2050 cm⁻¹^[50,54] These two values are in good agreement with the ones observed here (2086 and 2033 cm⁻¹). Another possibility is the adsorption of CO on terraces (higher frequency band at 2086 cm⁻¹), steps, and defects (lower frequency band at 2033 cm⁻¹).^[29,30,55]

2.4. CO Oxidation on Platinum

The behavior of the nano-slot metasurface was evaluated during the electrochemical oxidation of carbon monoxide using electrochemical cyclic voltammetry. The anodic scan in CO-saturated electrolyte presents an initial state with a low current (Figure 4a, black line). When an applied potential of ≈550 mV_{RHE} is reached, the current density plateaus at around +25 μA cm⁻², which is attributed to CO oxidation which can be written as^[56,57]



where * is a free adsorption site on platinum, CO_{ad} and OH_{ad} correspond to adsorbed CO and OH on Pt, respectively. At ca.

1150 mV_{RHE} the current density starts to decrease. The origin of this decrease is still debated in the literature. One explanation attributes the decreasing current density to competing adsorption of CO and OH on the Pt surface at higher potentials.^[58] Another possibility discussed is that the formation of a thin oxide or hydroxide Pt layer prevents the oxidation of CO. The latter assumption is supported by the reduction dip (from 860 to 620 mV_{RHE}) of platinum in argon-saturated electrolyte (Figure 4a,b). The behavior of the cathodic scan is similar, except that the onset of CO oxidation is shifted to more negative potentials resulting in a hysteresis. Moreover, a shift in the onset of the hydrogen evolution reaction in Ar^{sat} and CO^{sat} electrolyte is observed, highlighting the poisoning behavior of adsorbed CO on the platinum surface.^[59]

Similarly to our Fourier-transform infrared (FTIR) measurements in CO^{sat} electrolyte under OCP (Figure 3c), two CO_{linear} peaks were also found during the electrochemical potential sweeps (Figure 4c,d). There is a spectral shift during the anodic and cathodic scan (between 50 and 550 mV_{RHE}) which is attributed to either a higher π-back-donation from the metal to CO^[38,60] and/or to the Stark effect. The Stark effect results from the interactions between the surface electric field and the dipole moment of the adsorbates.^[60–62] During the anodic scan (Figure 4e), the most intense peak shows a blue shift of 53 cm⁻¹ V⁻¹ in agreement with the literature.^[36–38,61,63] The second peak shows a blueshift of 33 cm⁻¹ V⁻¹. Between 650 and 750 mV_{RHE} a redshift is observed which is not well documented in the literature.^[37,55,60,64] The redshift is attributed to a decrease of the CO coverage due to its oxidation into CO₂, decreasing the dipole-dipole interactions.^[55,65] The observation of the coverage effect was possible here due to the high resolution reached with the nano-slot metasurface. It was not resolved with a continuous platinum film. At higher anodic potentials, the CO_{linear} peaks disappeared due to CO oxidation. Since CO only oxidizes at the Pt surface the electrolyte remains saturated with CO highlighting that there is no contribution of dissolved CO to the IR signal. During the anodic scan, there is a slight increase in the area of the first peak (≈2033 cm⁻¹), while the area of the second peak slightly decreases. This behavior could be explained by a surface migration of adsorbed CO to a more stable position.^[31,37,38,52] Alternatively, the reconstruction or roughening of the Pt surface with electrical polarization^[66,67] could lead to a modification of the surface microstructure and CO adsorption energy.^[68] Looking at spectra obtained during the cathodic scan (Figure 4f), the second peak (≈2086 cm⁻¹) almost disappeared. This supports the assumption that the cause is the platinum surface modification at high applied potentials. At high cathodic potentials (150 to 50 mV_{RHE}) a decrease of the CO peak is observed and attributed to the hydrogen evolution reaction,^[63] indicating that the adsorption of hydrogen displaces adsorbed CO.

3. Conclusion

To the best of our knowledge, we have developed the first hybrid nanophotonic-electrochemical platform for SEIRAS based on a platinum nano-slot metasurface. The resonance of the metasurface was numerically modeled giving a maximum electric

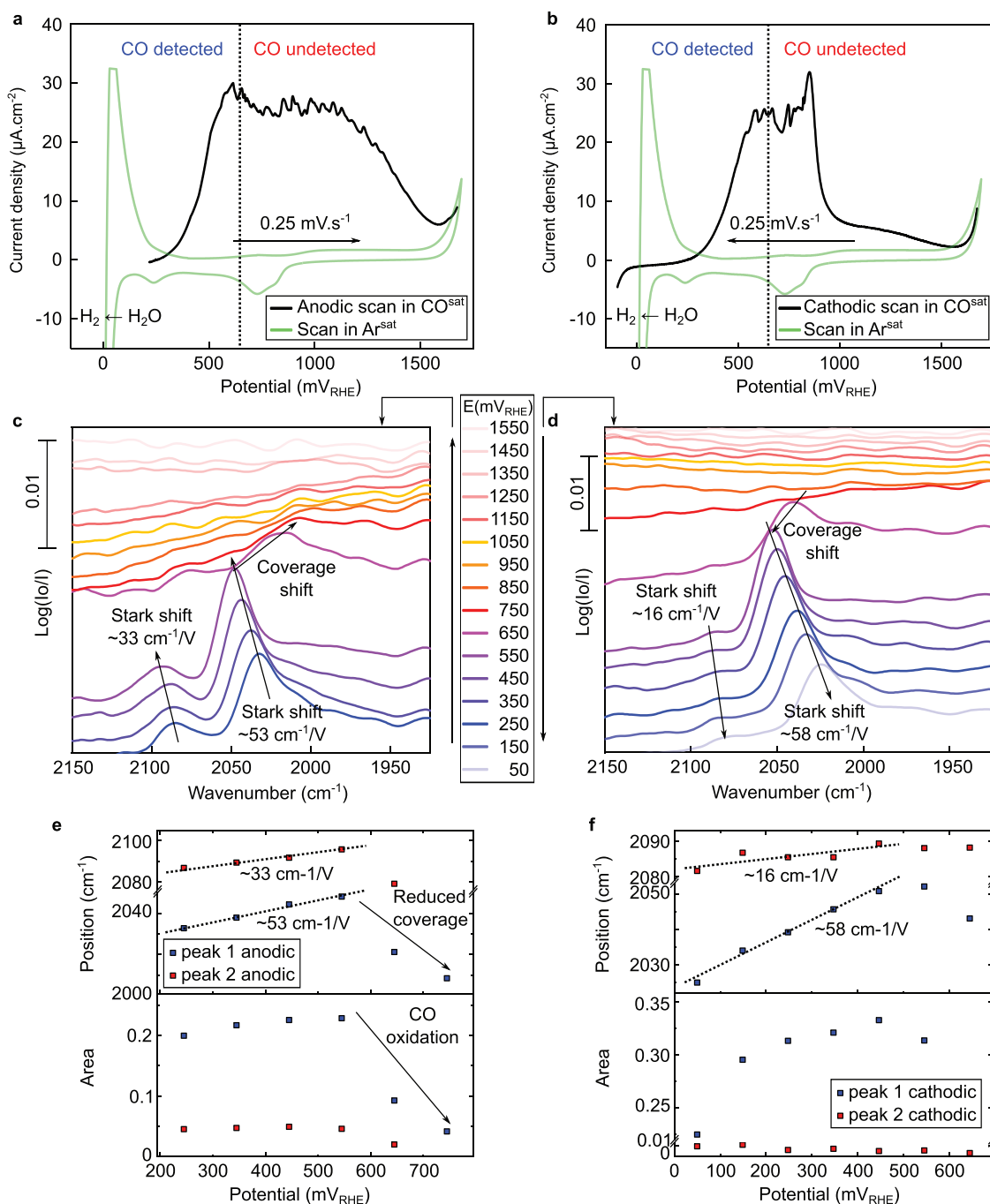


Figure 4. Behavior of the Pt nano-slot metasurface during cyclic voltammetry in $0.5\text{M K}_2\text{CO}_3$ saturated with CO at 0.25 mV s^{-1} . Evolution of the current density with the potential during the a) anodic (from OCP to $1700\text{ mV}_{\text{RHE}}$) and b) cathodic (from 1700 to $-100\text{ mV}_{\text{RHE}}$) scan in CO^{sat} electrolyte (black line). For comparison, the green line depicts cyclic voltammetry scans in an Ar^{sat} electrolyte. Evolution of SEIRAS spectra using s-polarized light with, the c) anodic and d) cathodic scans acquired every 100 mV . Evolution of the position and area of the $\text{CO}_{\text{linear}}$ peaks during the e) anodic and f) cathodic scans.

near-field intensity enhancement of 560. The resonance was tuned to couple with and enhance the CO vibrational mode at 2033 cm^{-1} . The principle behind the sensing improvement due to the electric near-field enhancement was tested by fabricating on-resonance and detuned metasurfaces and carefully analyzing the resonance. The numerical simulations and SEIRAS experimental results were in good agreement. Two peaks were

resolved for $\text{CO}_{\text{linear}}$ which could be attributed to adsorption of CO on Pt(111) and Pt(100). The vibrational mode of $\text{CO}_{\text{linear}}$ was best observed with a spectrally overlapping resonance leading to an experimental signal improvement of more than 27 over a conventionally used platinum film. During the electrochemical oxidation of CO, a classic Stark effect was observed. Moreover, thanks to the high resolution provided by the nano-slot

metasurface, a redshift of the vibrational mode of $\text{CO}_{\text{linear}}$ was observed, linked to a decrease of the coverage of adsorbed CO due to its oxidation. We anticipate our proof-of-concept nanophotonic-electrochemical platform for SEIRAS to guide new system designs and material combinations suitable to characterize different electrochemical interfaces, reaction products, and short-lived intermediates.

4. Experimental Section

Numerical Simulations: The simulations were performed in CST Studio Suite 2021 using the finite-element frequency-domain Maxwell solver. CaF_2 was simulated using a refractive index, n , of 1.4, the surrounding medium as water with $n = 1.33$ and platinum using the data given by Rakić et al.^[69] The inside walls perpendicular to the electric field were covered with a model material to represent the vibrational mode of $\text{CO}_{\text{linear}}$ at $\approx 2033 \text{ cm}^{-1}$ (see Supporting Information for more details). The titanium adhesion layer was not simulated as including it did not lead to substantial spectral shifts in the resonance position. An impedance-matched open port with a perfectly matched layer introduced linearly polarized light at an angle of 72° across the CaF_2 layer towards the nano-slots. At 72° the light was internally reflected at the CaF_2 -Pt interface. Therefore, the boundary opposite the open port was set as perfect electric conductor. The unit cell was defined and then simulated as an infinite periodic array via Floquet boundaries. A field monitor was placed at the center of the slot in the xy -plane. The highest field enhancement is found slightly above the apex of the slots. The value of the highest field enhancement of the system was evaluated within the volume of the numerical model. To extract the Q-factor and coupling ratio γ_e/γ_r , the simulated resonance was fitted in reflectance (Figure 1d, blue curve) using temporal coupled mode theory according to Hu et al.^[70]

Metasurface Fabrication: CaF_2 was selected as the substrate due to its transparent nature in the mid-IR spectral range, low solubility, and high chemical stability. The measurements shown in Figures 3 and 4 used metasurface arrays with at least 2200 by 2700 unit cells resulting in a pattern area of approximately 13.3 mm^2 , which ensured that there are more than enough unit cells for the measured resonance to correspond to the mode of the infinite periodic array used for the numerical simulations. After sample cleaning (acetone bath in an ultrasonic cleaner followed by oxygen plasma cleaning) the substrate was spin-coated first with an adhesion promoter (Surpass 4000), then with a layer of negative tone photoresist (ma-N 2403) which was baked at 100°C for 60 s, and finally with a conducting layer (ESpacer 300Z). The metasurface patterns were created by defining the unit cell and reproducing it in the x and y -directions. Then, the patterns were written via electron-beam lithography (Raith Eline Plus) with an acceleration voltage of 30 kV and an aperture of $20 \mu\text{m}$. The exposed resist was developed in ma-D 525 for 70 s at room temperature. The patterned surface was then coated with a titanium adhesion layer (1 nm at 0.4 \AA s^{-1}) and a platinum film (30 nm at 2 \AA s^{-1}) using electron-beam evaporation (PRO Line PVD 75, Lesker). Finally, an overnight lift-off in mr-REM 700 concluded the top-down fabrication process. A pure 30 nm thick platinum film on 1 nm titanium on CaF_2 functioned as a reference for the in situ SEIRAS measurements.

In Situ SEIRAS and Electrochemical Measurements: SEIRAS was performed using a Vertex 80 coupled with an IMAC chamber from Bruker. Each sample was mounted on a VeeMax III (purged with nitrogen) from PIKE Technologies in attenuated total internal reflection (ATR) mode with a light polarizer, an electrochemical Jackfish cell, and a CaF_2 prism beveled at 72° . A classical three-electrode system was used with a Saturated Calomel Electrode ($E = 0.244 \text{ V}_{\text{SHE}}$), a platinum wire as counter electrode, and the platinum sample as working electrode. The IMAC chamber is equipped with a focal plane array detector composed of 64×64 MCT-detectors (a total of 4096 detectors), which allows to perform a mapping of the studied sample. Each detector collects its own spectrum and then, the active slot covered area is detected by

integration of each spectrum between 1600 to 2800 cm^{-1} (Figure 3b, inset). Finally, an average can be determined using the spectra of the detectors that probed the resonance. A baseline correction is applied to this average as well as a Savitzky–Golay filter to smoothen the data.

For the characterization of the resonance, its position was determined using three samples composed of arrays with different nanostructure sizes. For each sample, the resonance was measured in K_2CO_3 (0.5 M , $\text{pH } 11.9$) electrolyte saturated with Ar and then saturated with CO. Prior to the first characterization, a cyclic voltammogram (20 mV s^{-1}) was recorded in order to confirm the cleanliness of the electrode surface. Then, an initial background was acquired using p-polarized light and the Fano resonance was characterized using s-polarized light. Each spectrum was recorded with a resolution of 4 cm^{-1} and the final mapping results from a collection of 32 scans. The enhancement of the nano-slot metasurface is obtained by comparison of the vibrational mode of $\text{CO}_{\text{linear}}$ on a pure Pt layer (30 nm) without nanostructures.

The adsorption of CO during the transition from Ar^{sat} to CO^{sat} electrolyte ($0.5 \text{ M K}_2\text{CO}_3$) was studied using the nano-slot metasurface with the best overlapping resonance with the vibrational mode of $\text{CO}_{\text{linear}}$. Cleaning and background acquisition protocols were the same as described above. Carbon monoxide slowly flowed into the electrochemical cell and spectra were acquired regularly during the transition from Ar^{sat} to CO^{sat} electrolyte at the OCP.

The oxidation of CO during potential sweeps was investigated after 2 h of CO bubbling. A cyclic voltammogram, with a slow scan rate (0.25 mV s^{-1}), from the OCP to $+1700 \text{ mV}_{\text{RHE}}$ and back to $-100 \text{ mV}_{\text{RHE}}$ was performed and a spectrum was acquired every 100 mV .

Supporting Information

Supporting Information is available from the Wiley Online Library or from the author.

Acknowledgements

The authors thank Thomas Weber for his help with the temporal-coupled mode theory algorithms and Simon Stork for the platinum and titanium electron beam evaporation. This work was funded by the Deutsche Forschungsgemeinschaft (DFG, German Research Foundation) under grant numbers EXC 2089/1–390776260 (Germany's Excellence Strategy) and TI 1063/1 (Emmy Noether Program), ERC-STG 802989 Catalight, the Bavarian program Solar Energies Go Hybrid (SolTech) and the Center for NanoScience (CeNS). S.A.M. additionally acknowledges the Lee-Lucas Chair in Physics and the EPSRC (EP/W017075/1).

Open access funding enabled and organized by Projekt DEAL.

Conflict of Interest

The authors declare no conflict of interest.

Author Contributions

L.M.B and M.D. contributed equally to this work. The manuscript was written through the contributions of all authors. All authors have given approval to the final version of the manuscript.

Data Availability Statement

The data that support the findings of this study are available from the corresponding author upon reasonable request.

Keywords

CO oxidation, in situ investigations, metasurfaces, nanophotonics, spectro-electrochemistry, surface-enhanced IR absorption spectroscopy

Received: January 11, 2023

Revised: February 21, 2023

Published online: March 20, 2023

- [1] M. F. Lagadec, A. Grimaud, *Nat. Mater.* **2020**, *19*, 1140.
- [2] I. Sullivan, A. Goryachev, I. A. Digdaya, X. Li, H. A. Atwater, D. A. Vermaas, C. Xiang, *Nat. Catal.* **2021**, *4*, 952.
- [3] I. E. L. Stephens, K. Chan, A. Bagger, S. W. Boettcher, J. Bonin, E. Boutin, A. K. Buckley, R. Buonsanti, E. R. Cave, X. Chang, S. W. Chee, A. H. M. da Silva, P. de Luna, O. Einsle, B. Endrődi, M. Escudero-Escribano, J. V. F. de Araujo, M. C. Figueiredo, C. Hahn, K. U. Hansen, S. Haussener, S. Hunegnaw, Z. Huo, Y. J. Hwang, C. Janáky, B. S. Jayathilake, F. Jiao, Z. P. Jovanov, P. Karimi, M. T. M. Koper, et al., *J. Phys. Energy* **2022**, *4*, 042003.
- [4] S. Zhao, R. Jin, R. Jin, *ACS Energy Lett.* **2018**, *3*, 452.
- [5] A. Wuttig, M. Yaguchi, K. Motobayashi, M. Osawa, Y. Surendranath, *Proc. Natl. Acad. Sci. USA* **2016**, *113*, E4585.
- [6] G. G. Hammes, *Spectroscopy for the Biological Sciences*, John Wiley & Sons, Hoboken, New Jersey, USA **2005**.
- [7] X. Yang, Z. Sun, T. Low, H. Hu, X. Guo, F. J. García de Abajo, P. Avouris, Q. Dai, *Adv. Mater.* **2018**, *30*, 1704896.
- [8] F. Neubrech, C. Huck, K. Weber, A. Pucci, H. Giessen, *Chem. Rev.* **2017**, *117*, 5110.
- [9] J. A. Ribeiro, M. G. F. Sales, C. M. Pereira, *TrAC Trends Anal. Chem.* **2022**, *157*, 116766.
- [10] S. Vijay, T. V. Hogg, J. Ehlers, H. H. Kristoffersen, Y. Katayama, Y. Shao Horn, I. Chorkendorff, K. Chan, B. Seger, *J. Phys. Chem. C* **2021**, *125*, 17684.
- [11] Y. Katayama, F. Nattino, L. Giordano, J. Hwang, R. R. Rao, O. Andreussi, N. Marzari, Y. Shao-Horn, *J. Phys. Chem. C* **2019**, *123*, 5951.
- [12] M. Dunwell, Q. Lu, J. M. Heyes, J. Rosen, J. G. Chen, Y. Yan, F. Jiao, B. Xu, *J. Am. Chem. Soc.* **2017**, *139*, 3774.
- [13] D. Wang, F. Shi, J. Jose, Y. Hu, C. Zhang, A. Zhu, R. Grzeschik, S. Schlücker, W. Xie, *J. Am. Chem. Soc.* **2022**, *144*, 5003.
- [14] D. Rodrigo, A. Tittl, N. Ait-Bouziad, A. John-Herpin, O. Limaj, C. Kelly, D. Yoo, N. J. Wittenberg, S.-H. Oh, H. A. Lashuel, H. Altug, *Nat. Commun.* **2018**, *9*, 2160.
- [15] A. Tittl, A. Leitis, M. Liu, F. Yesilkoy, D.-Y. Choi, D. N. Neshev, Y. S. Kivshar, H. Altug, *Science* **2018**, *360*, 1105.
- [16] S. A. Hosseini Farahabadi, M. Entezami, H. Abouali, H. Amarloo, M. Poudineh, S. Safavi-Naeini, *Sci. Rep.* **2022**, *12*, 17747.
- [17] T. Li, D. Shang, S. Gao, B. Wang, H. Kong, G. Yang, W. Shu, P. Xu, G. Wei, *Biosensors* **2022**, *12*, 314.
- [18] J. Wang, S. A. Maier, A. Tittl, *Adv. Opt. Mater.* **2022**, *10*, 2102366.
- [19] J. Jiang, X. Wang, S. Li, F. Ding, N. Li, S. Meng, R. Li, J. Qi, Q. Liu, G. L. Liu, *Nanophotonics* **2018**, *7*, 1517.
- [20] N. Li, Y. Lu, S. Li, Q. Zhang, J. Wu, J. Jiang, G. L. Liu, Q. Liu, *Biosens. Bioelectron.* **2017**, *93*, 241.
- [21] K. Nakamoto, R. Kurita, O. Niwa, *Anal. Chem.* **2012**, *84*, 3187.
- [22] X. Wang, S.-C. Huang, S. Hu, S. Yan, B. Ren, *Nat. Rev. Phys.* **2020**, *2*, 253.
- [23] D. Wright, Q. Lin, D. Berta, T. Földes, A. Wagner, J. Griffiths, C. Readman, E. Rosta, E. Reisner, J. J. Baumberg, *Nat. Catal.* **2021**, *4*, 157.
- [24] Y. Fang, H. Wang, H. Yu, X. Liu, W. Wang, H.-Y. Chen, N. J. Tao, *Acc. Chem. Res.* **2016**, *49*, 2614.
- [25] X. R. Cheng, G. Q. Wallace, F. Lagugné-Labarthe, K. Kerman, *ACS Appl. Mater. Interfaces* **2015**, *7*, 4081.
- [26] S.-S. Wang, X.-P. Zhao, F.-F. Liu, M. R. Younis, X.-H. Xia, C. Wang, *Anal. Chem.* **2019**, *91*, 4413.
- [27] E. Cortés, F. J. Wendisch, L. Sortino, A. Mancini, S. Ezendam, S. Saris, L. S. de Menezes, A. Tittl, H. Ren, S. A. Maier, *Chem. Rev.* **2022**, *122*, 15082.
- [28] A. Stefanu, L. Nan, L. Zhu, V. Chiş, I. Bald, M. Liu, N. Leopold, S. A. Maier, E. Cortes, *Adv. Opt. Mater.* **2022**, *10*, 2200397.
- [29] M. J. Hossain, M. M. Rahman, M. d. J. Sharif, *Nanoscale Adv.* **2020**, *2*, 1245.
- [30] C. D. Silva, G. Cabello, W. A. Christinelli, E. C. Pereira, A. Cuesta, *J. Electroanal. Chem.* **2017**, *800*, 25.
- [31] I. J. McPherson, P. A. Ash, L. Jones, A. Varambhia, R. M. J. Jacobs, K. A. Vincent, *J. Phys. Chem. C* **2017**, *121*, 17176.
- [32] A. Susarrey-Arce, R. M. Tiggelaar, J. G. E. Gardeniers, A. van Houselt, L. Lefferts, *J. Phys. Chem. C* **2015**, *119*, 24887.
- [33] T. Smolinka, M. Heinen, Y. X. Chen, Z. Jusys, W. Lehnert, R. J. Behm, *Electrochim. Acta* **2005**, *50*, 5189.
- [34] Y. Katayama, L. Giordano, R. R. Rao, J. Hwang, H. Muroyama, T. Matsui, K. Eguchi, Y. Shao-Horn, *J. Phys. Chem. C* **2018**, *122*, 12341.
- [35] C. Huck, J. Vogt, M. Sendner, D. Hengstler, F. Neubrech, A. Pucci, *ACS Photonics* **2015**, *2*, 1489.
- [36] I. Villegas, M. J. Weaver, *J. Chem. Phys.* **1994**, *101*, 1648.
- [37] S. Watanabe, J. Inukai, M. Ito, *Surf. Sci.* **1993**, *293*, 1.
- [38] M. Nakamura, H. Ogasawara, J. Inukai, M. Ito, *Surf. Sci.* **1993**, *283*, 248.
- [39] I. Hickman, *Analog Electronics: Analog Circuitry Explained*, Elsevier, Amsterdam, Netherlands, **2013**.
- [40] H. Gao, J. M. McMahon, M. H. Lee, J. Henzie, S. K. Gray, G. C. Schatz, T. W. Odom, *Opt. Express* **2009**, *17*, 2334.
- [41] R. Adato, A. A. Yanik, C.-H. Wu, G. Shvets, H. Altug, *Opt. Express* **2010**, *18*, 4526.
- [42] R. Adato, A. Artar, S. Erramilli, H. Altug, *Nano Lett.* **2013**, *13*, 2584.
- [43] A. Aigner, A. Tittl, J. Wang, T. Weber, Y. Kivshar, S. A. Maier, H. Ren, *Sci. Adv.* **2022**, *8*, eadd4816.
- [44] J. Lan, J. Hutter, M. Iannuzzi, *J. Phys. Chem. C* **2018**, *122*, 24068.
- [45] J. Kühne, J. Wang, T. Weber, L. Kühner, S. A. Maier, A. Tittl, *Nanophotonics* **2021**, *10*, 4305.
- [46] M. J. S. Farias, C. Busó-Rogero, A. A. Tanaka, E. Herrero, J. M. Feliu, *Langmuir* **2020**, *36*, 704.
- [47] B. Luk'yanchuk, N. I. Zheludev, S. A. Maier, N. J. Halas, P. Nordlander, H. Giessen, C. T. Chong, *Nat. Mater.* **2010**, *9*, 707.
- [48] S. Fan, *Appl. Phys. Lett.* **2002**, *80*, 908.
- [49] R. H. A. Ras, R. A. Schoonheydt, C. T. Johnston, *J. Phys. Chem. A* **2007**, *111*, 8787.
- [50] A. Cuesta, A. Couto, A. Rincón, M. C. Pérez, A. López-Cudero, C. Gutiérrez, *J. Electroanal. Chem.* **2006**, *586*, 184.
- [51] A. López-Cudero, A. Cuesta, C. Gutiérrez, *J. Electroanal. Chem.* **2005**, *579*, 1.
- [52] S.-G. Sun, Z.-Y. Zhou, *Phys. Chem. Chem. Phys.* **2001**, *3*, 3277.
- [53] A. Rodes, E. Pastor, T. Iwasita, *J. Electroanal. Chem.* **1994**, *377*, 215.
- [54] A. López-Cudero, Á. Cuesta, C. Gutiérrez, *J. Electroanal. Chem.* **2006**, *586*, 204.
- [55] S.-C. Chang, M. J. Weaver, *Surf. Sci.* **1990**, *230*, 222.
- [56] B. B. Bliznac, C. A. Lucas, M. E. Gallagher, M. Arenz, P. N. Ross, N. M. Marković, *J. Phys. Chem. B* **2004**, *108*, 625.
- [57] N. Mayet, K. Servat, K. B. Kokoh, T. W. Napporn, *Electrocatalysis* **2021**, *12*, 26.
- [58] J. S. Spendlow, J. D. Goodpaster, P. J. A. Kenis, A. Wieckowski, *J. Phys. Chem. B* **2006**, *110*, 9545.
- [59] A. S. Varela, C. Schlaup, Z. P. Jovanov, P. Malacrida, S. Horch, I. E. L. Stephens, I. Chorkendorff, *J. Phys. Chem. C* **2013**, *117*, 20500.

- [60] G. Samjeské, K. Komatsu, M. Osawa, *J. Phys. Chem. C* **2009**, *113*, 10222.
- [61] Y. Katayama, L. Giordano, R. R. Rao, J. Hwang, H. Muroyama, T. Matsui, K. Eguchi, Y. Shao-Horn, *J. Phys. Chem. C* **2018**, *122*, 12341.
- [62] V. Stamenkovic, K. C. Chou, G. A. Somorjai, P. N. Ross, N. M. Markovic, *J. Phys. Chem. B* **2005**, *109*, 678.
- [63] M. Dunwell, J. Wang, Y. Yan, B. Xu, *Phys. Chem. Chem. Phys.* **2017**, *19*, 971.
- [64] M. Dunwell, Y. Yan, B. Xu, *ACS Catal.* **2017**, *7*, 5410.
- [65] P. Deshlahra, J. Conway, E. E. Wolf, W. F. Schneider, *Langmuir* **2012**, *28*, 8408.
- [66] L. Jacobse, M. J. Rost, M. T. M. Koper, *ACS Cent. Sci.* **2019**, *5*, 1920.
- [67] X. Deng, F. Galli, M. T. M. Koper, *ACS Appl. Energy Mater.* **2020**, *3*, 597.
- [68] B. Hammer, O. H. Nielsen, J. K. Nørskov, *Catal. Lett.* **1997**, *46*, 31.
- [69] A. D. Rakić, A. B. Djurišić, J. M. Elazar, M. L. Majewski, *Appl. Opt.* **1998**, *37*, 5271.
- [70] H. Hu, T. Weber, O. Bienek, A. Wester, L. Hüttenhofer, I. D. Sharp, S. A. Maier, A. Tittel, E. Cortés, *ACS Nano* **2022**, *16*, 13057.